ACS MATERIALS LETTERS

Volume 6, Issue 6 June 2024 pubs.acs.org/materialslett

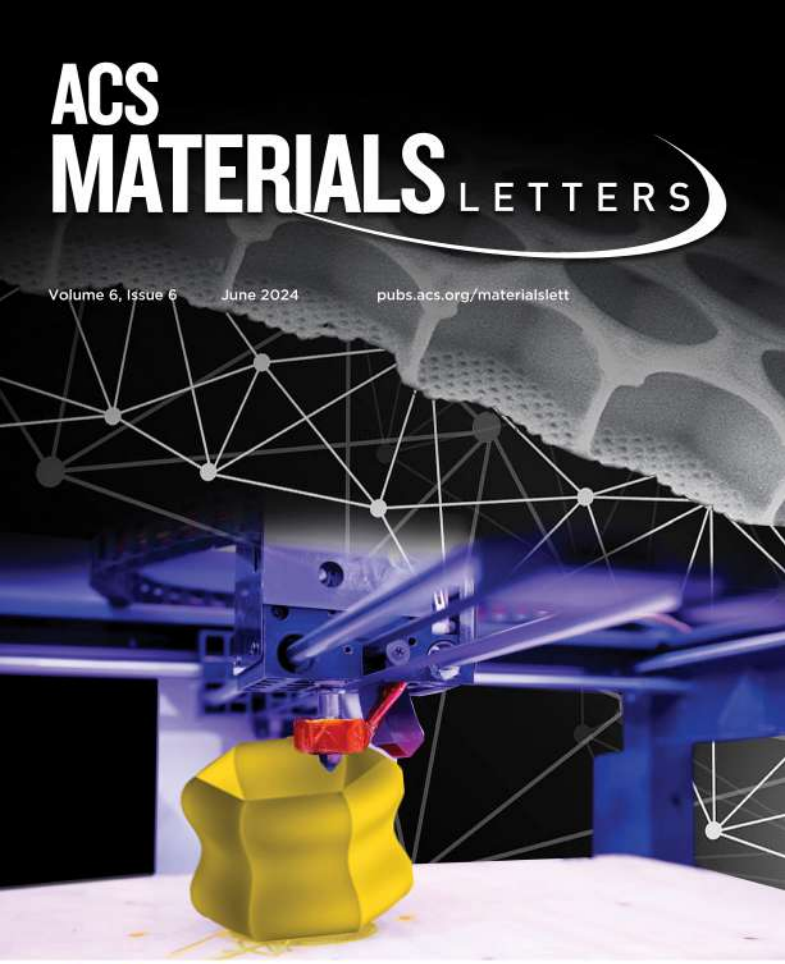

ACS Publications
Most Trusted. Most Cited. Most Read.

www.acs.org

Tunable energy absorption in 3D-printed data-driven diatom-inspired architected materials

Ludovico Musenich, Alessandro Stagni, Lucio Derin, Flavia Libonati*

University of Genoa, Polytechnic School, Department of Mechanical, Energy, Management and Transportation Engineering (DIME-MEC), Via all'Opera Pia 15/A, 16145, Genova, Italy

ABSTRACT: Boosted by additive manufacturing, architected materials have opened new opportunities to extend the performance of engineering materials. Yet, their development is held back by the intense efforts required to understand their complex property-structure-process-performance relationship. Therefore, data-driven biomimetic approaches are becoming increasingly popular to unveil such relationships. Here we mimic the functionally graded structures found in Coscinodiscus sp. diatom to understand the role of their shapes and define new guidelines for the design of novel architected honeycombs with tunable mechanical properties. Finite element simulations, validated on the outcome of a testing campaign performed on 3D-printed elastomeric samples, are used to build a dataset for machine learning algorithm training. Different machine learning techniques are used to link the geometric features of the designed biomimetic structures to their energy absorption properties and, in particular, to the specific absorbed energy divided by the peak force, here used as the performance index. The proposed approach leads to a novel design, which features a performance increase of 250% w.r.t. conventional honeycombs.

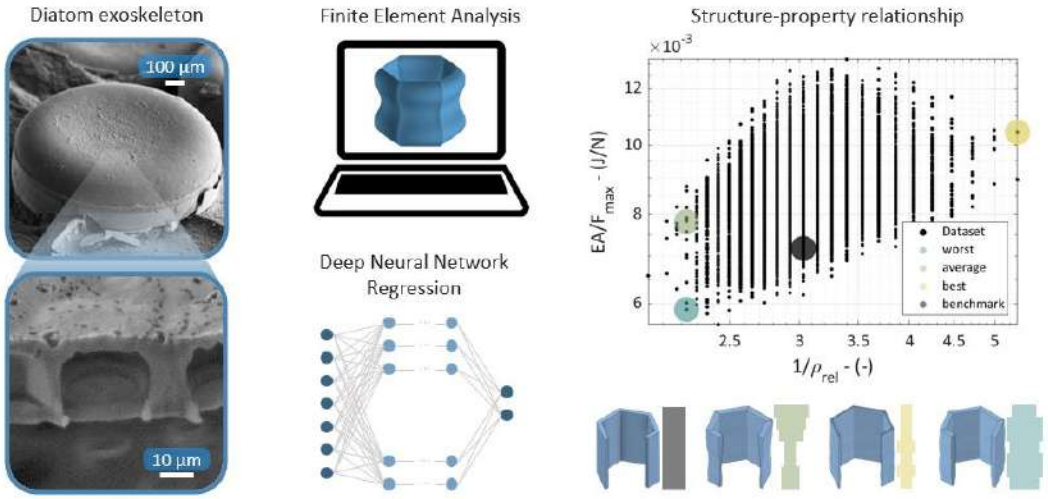

Architected materials are a class of materials in which chemical and geometrical features are carefully controlled on different length scales to ensure the optimal accomplishment of specific tasks. Typical examples are honeycombs, strut-based lattices, and triply periodic minimal surface lattices[1,2]. Their power lies in the ability to tune their performance by acting on the hierarchical and mutual interplay between material and structure. Thus, they find application in a multitude of fields, such as lightweight structures, wave propagation control, bio-scaffolds, and sensing[2–4].

Advances related to architected materials have been mainly driven by the mimicry of natural materials like bone, wood, nacre, and diatoms[5–11], whose remarkable capabilities and multifunctionality are mainly attributed to the sophisticated multiscale hierarchical structure[12,13], despite the limited palette of building blocks they are made of. In Nature, a few universal building blocks, combined into common structural arrangements, functional gradients, and interfaces with recurring patterns over multiple length scales[5,14–20] lead to a wide diversity of structures and materials, able to meet different functions and needs. Today, thanks to imaging techniques, numerical simulations, and additive manufacturing (AM), the application of the "universality-diversity" paradigm found in Nature[21–23] to the design of architected materials has turned out to be a very fruitful guide[23–27]. Yet, unraveling the property-structure-process-performance relationship[28] and transferring it to a man-made material is generally a non-straightforward highly resource-intensive process. In recent years, data-driven approaches, especially machine learning (ML), have proven to be valuable methods to overcome this issue[29–34]. ML algorithms have been successfully used for the data-driven design of new materials by: (i) replacing constitutive equations for the analysis of new material properties, (ii) identifying new material architectures, (iii) guiding the choice of process parameters, and (iv) improving performance such as fatigue life, buckling resistance, and fracture toughness[29–34]. Latest cutting-edge research has demonstrated that Materials Informatics tools at the forefront, such as attention-

based diffusion models[35] and multi-modal language models[36], are capable of both providing forward predictions (*i.e.*, obtaining nonlinear structural behaviors as a function of material hierarchical structure) and effectively solving inverse design problems (*i.e.*, discover new architectures that have specified response curves), giving increasing room for customization of material representations and offering ever-expanding generalization capabilities (*i.e.*, the same models can be applied to different materials, dimensional scales, and design tasks). While biomimicry has been successfully used to provide design solutions for materials with superior mechanical properties, ML-based methods have further accelerated the design process and the discovery of new materials[37].

Inspired by the fascinating diatom morphology[38–42], in this research we propose a biomimetic data-driven approach for the design of novel architected honeycombs with tunable energy absorption performances. What caught our attention on these aquatic algae is the organization of the amorphous biosilica that forms the exoskeleton, aka frustule. The frustule of Coscinodiscus sp. diatoms exhibits a hierarchical architected design, consisting of three main layers: (i) cribrum, (ii) areolae, and (iii) foramen (Figure 1). From a structural point of view, this protective shell is designed to withstand predatory attacks that result in compressive loads. It provides both lightness and mechanical protection at the same time, and the central honeycomb-like layer is the one that affects such performance the most[41,43–49]. Previous AI diatom-based designs focused on a publicly available diatom dataset to translate their intriguing structural features into 3D printable material models, showing the great potential offered by the intersection of human and artificial intelligence to generate innovative biologically inspired design solutions[50]. Here, we start from solutions offered by Nature and investigate the relationship between their shapes and mechanical properties. Specifically, an intriguing feature of Coscinodiscus diatoms is the cell wall profile of the areolae, which shows varying thickness gradients (Figure 1 (b)), not observed in other natural and synthetic honeycombs. This research work arises from the need to answer the following questions: what role does it play in determining the overall properties of the frustule? Can we tune the shape of the cell walls to improve the mechanical performance of bioinspired architected materials? The deformation of honeycombs under out-of-plane compression is mainly governed by buckling-induced collapse. Thus, this failure mode, typically detrimental, could be harnessed to adapt the material's energy absorption properties according to the specific application of interest.

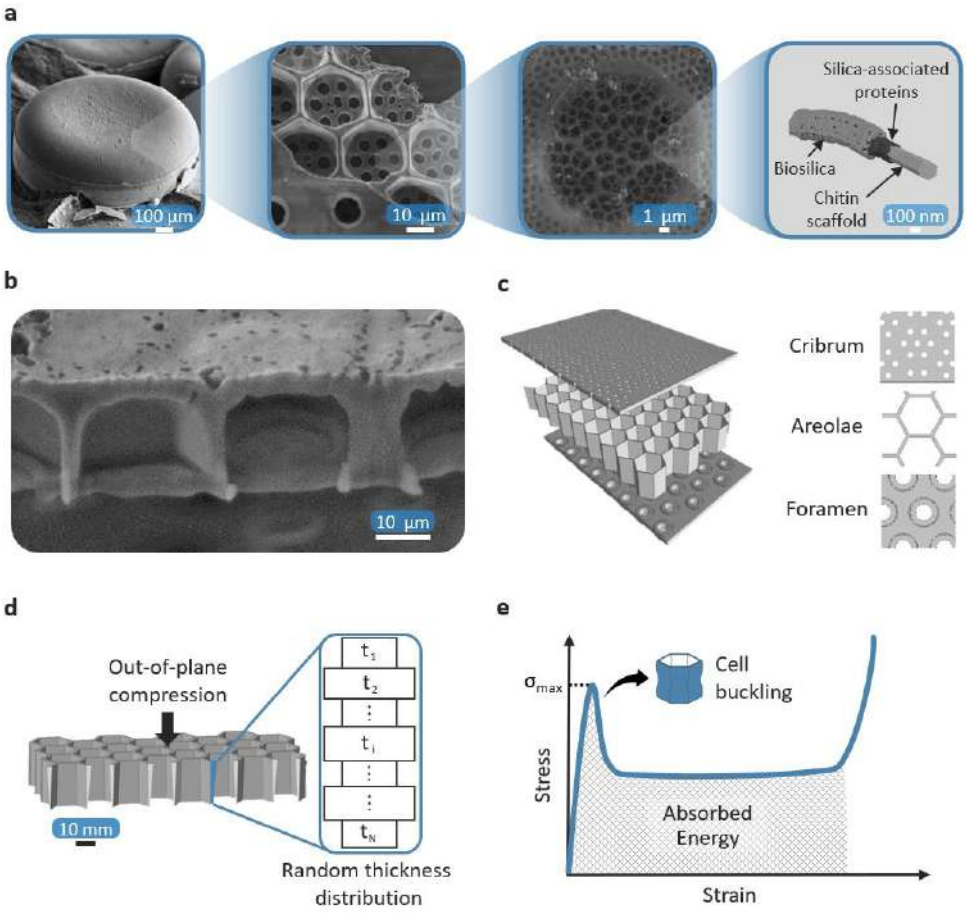

Figure 1. Hierarchical architecture of the studied diatom frustule, schematization, geometric, and numerical model. (a) Hierarchical architecture of the Coscinodiscus sp. diatom frustule with its four different levels: "Petri dish" configuration shared by all diatoms (modified from[39], CC BY 4.0); sandwich-like structure distinctive for this family of

diatoms (modified from[51]); intricate porous network of amorphous silica that covers the entire outer surface of the frustule (modified from[51]); building blocks that make up the frustule (modified from[52], CC BY 4.0). (b) Cross-section of the Coscinodiscus sp. diatom multilayer exoskeleton: view of the thickness gradient present in the cell walls of its honeycomb substructure (modified from[39], CC BY 4.0). (c) Simplified geometric model of the sandwich-like structure of the Coscinodiscus sp. frustule with its three layers: cribrum, areolae, and foramen. (d) Schematic representation of the thickness gradient in the analyzed honeycomb-like structures (e) Example of the stress-strain response curve of elastomeric honeycombs under out-of-plane compression.

Before the advent of AM, it was impossible to fabricate structures with such a level of complexity, so the effect of functional gradients in honeycomb walls has not been fully investigated yet. Previous studies have highlighted that the spatial tailoring of honeycomb geometry can substantially enhance their performance and be exploited for fine-tuning their properties. Regarding the in-plane mechanics of honeycombs, in particular, the use of deep learning models has enabled control over the material distribution in their cellular walls through encoded patterns to generate innovative designs that provide designer-specified nonlinear constitutive relationships[35,36]. The out-of-plane behavior has been partially analyzed, focusing on simple material distribution laws [53,54].

In this study, we leverage ML techniques, finite element analysis (FEA), and AM to deeply delve into the effect of thickness gradients on the out-of-plane honeycomb mechanical performance. Given the diversity of shapes and gradients occurring in the Coscinodiscus sp. diatom frustule[38,40,41], we focus the study on a single hexagonal prismatic cell. A large dataset of bioinspired digital models of diatom geometry is created. A subset is adopted to generate a numerical dataset describing the relationship between the cell shape and its mechanical performance (*i.e.*, the out-of-plane compression properties calculated by FEA). Based on simulation outcomes, supervised learning algorithms are trained for regression and the design space is extensively explored by using the best metamodel. A comprehensive parameter, based on critical load, absorbed energy, and density of each bioinspired honeycomb cell, is used for performance analysis and topology ranking. Finally, AM and testing are exploited for the validation of the proposed data-driven designs. This bioinspired ML-driven approach allows one to identify an ideal structure for protective gear applications, featuring a 250% boost in energy absorption capability compared to a classic honeycomb unit cell with constant wall thickness. Moreover, the proposed framework, based on ML and AM, represents a versatile, powerful, and sustainable approach, which accelerates the design phase and expands the design space by orders of magnitude compared to conventional methods, considerably reducing the resources, time, and costs involved in simulations, manufacturing, and testing.

Numerical model validation. Driven by the growing interest in "multi-hit" devices for mechanical energy absorption[55], we focus on the geometry of the honeycomb-like architectures found in Coscinodiscus sp. diatoms and use a thermoplastic polyurethane (TPU), instead of the natural biosilica, as parent material. This choice is driven by the fact that (i) elastomeric materials are typically used in energy absorption applications, (ii) TPU is easily available for AM technology. To have a reliable dataset for the ML algorithm training, the finite element (FE) model, used to generate the synthetic data, is validated analytically and experimentally. The analytical formulae based on honeycomb mechanics give us a first approximation, and then the numerical model is validated on a single honeycomb unit cell with constant wall thickness taken as a benchmark. According to experimental test results of 3D-printed samples, the Blatz-Ko hyperelastic model is calibrated to replicate the non-linear behavior of the material.

Figure 2 (a) shows the comparison among data obtained from the three approaches used. The unit cell is analyzed without considering the periodicity of the architected material. Figure 2 (b-d) depicts the theoretical, simulated, and physically observed deformation modes. In the elastic region there is an optimal match between the numerical and experimental curves, with a difference of 11.3% in terms of compression modulus. The experimental test results are very similar to the one predicted by the FEA and the analytical formulae, showing an error of 2.1% and 0.8% on the maximum stress, respectively. In general, there is a good comparison in terms of elastic modulus of compression, peak stress, and absorbed energy. A more quantitative comparison is provided in Table 1.

It should be noted that the calculation of elastic moduli is very sensitive to the selected strain range, so the errors related to it are less meaningful than those associated with the other mechanical properties evaluated. Beyond the maximum stress, the finite element model becomes stiffer and deviates from what is measured experimentally. This difference is primarily due to the anisotropies and imperfections introduced by the AM process in the testing specimens, and it also affects the structure deformation mode. The height of the benchmark cell is twice its side. From the theory of elastic stability we expect, in each of its walls, two whole deformational half-waves in the vertical direction and only one in the direction perpendicular to it[56]. The 3D printed cell (Figure 2 (d)) shows a shift of such deformation waves and shapes that are not perfectly harmonic w.r.t. the theoretical and numerical counterparts.

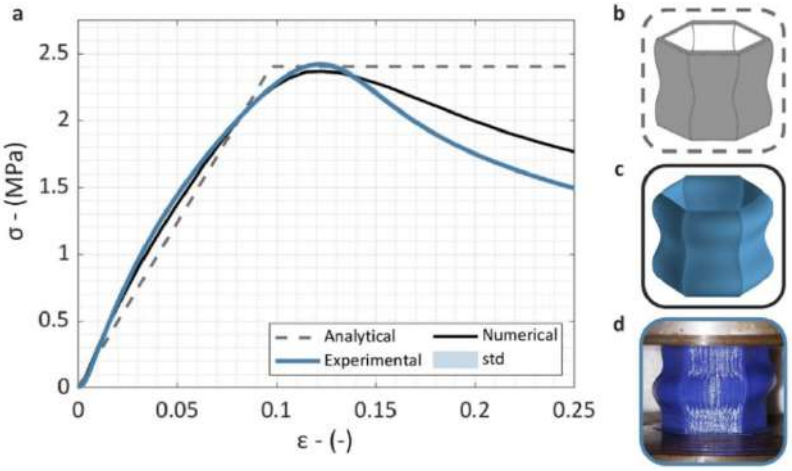

Figure 2. Finite element model validation. (a) Analytical, numerical, and experimental comparison of the response curve of the benchmark honeycomb cell with constant-thickness walls in out-of-plane compression. Cell deformation modes according to (b) honeycomb mechanics, (c) numerical simulations based on FEA, and (d) experimental compression test.

Table 1. Mechanical properties of the honeycomb cell with a constant-thickness wall calculated analytically, numerically, and experimentally. Elastic modulus is calculated between 0.01 and 0.03 strain. Percent errors are calculated with respect to experimental results ("ground truth").

Parameter	Unit	Experimental	Numerical	err %	Analytical	err %
Elastic Modulus	MPa	33.27	29.50	11.3%	24.74	25.7%
Maximum stress	MPa	2.42	2.37	2.1%	2.40	0.8%
Specific absorbed energy	J/mm^3	0.432	0.45	3.6%	0.49	12.2%

Metamodel Selection. After the FE model validation, a numerical dataset is built. This dataset, which includes about one tenth of all the generated structures populating the design space, is solved numerically via FEA to determine the mechanical behavior of such structures. This dataset is used for training, tuning, and testing three different supervised machine learning algorithms to determine an optimal metamodel capable of predicting the maximum force F_{max} (*i.e.*, the critical load) and absorbed energy, EA, of each cell model within the design space, based on knowledge of the material distribution along their walls. Specifically, a Linear Ridge Regression (LRR), a Kernel Ridge Regression (KRR), and a Deep Neural Network (DNN) are used. Figure 3 shows the comparison between the distributions of the target mechanical properties calculated numerically and predicted using ML for all the structures present in the test set. LRR is too simple to capture the nonlinear phenomena involved in the out-of-plane compression of elastomeric honeycomb cells. Better results are achieved with KRR and DNN with R^2 scores of 0.964 and 0.981, respectively (see Table 2). Furthermore, it is worth noting that both KRR and DNN predict the same best-performing structure on the validation and test sets. Although the prediction accuracy for KRR and DNN are similar, with KRR being 250 times faster than DNN in terms of training time (0.3 seconds compared to 75 seconds), the DNN is selected to explore the remaining portion of the design space (*i.e.*, predicting the performance of structures not included in the dataset). This decision is motivated by the DNN's stronger correlation in distribution tails, meaning its ability to confidently predict the outliers. Furthermore, once trained, it is $\sim 10^5$ faster than FEA in calculating the honeycomb cell mechanical properties, thus it significantly facilitates the design space exploration process. Details regarding its tuning, performance, and the hardware resources employed for its utilization are described in the Supporting Information (SI).

Effect of thickness gradients on energy absorption properties. In energy absorption applications the choice of material is usually guided by (i) the amount of energy to be dissipated, (ii) the maximum stress associated with it, and (iii) the weight limits imposed by the product design[57]. To rank the analyzed structures, a performance parameter, based on the energy absorbed divided by the maximum force of each cell and by the relative density ρ_{rel}, is used. Figure 4 (a) shows the results obtained for our design space. A significant variability in mechanical properties is observed from the graph. From the theory of constant-wall honeycombs, we expect an increase of the critical load according to the mass of the cell walls, thus their stiffness. Intuitively one might assume a monotonic trend between EA/F_{max} and ρ_{rel}. However, such trend cannot be found in the results because the shape variations, featured in the bioinspired cells,

significantly affect both the buckling load and the energy absorption mode following the collapse of the cell due to instability (*i.e.*, the post-buckling behavior).

To understand the effect of thickness gradients, three structures, representative of this variability, are selected and compared with the benchmark model. Specifically, the honeycomb cell models with geometric tailoring are characterized by: (i) the best mechanical performance, (ii) the worst mechanical performance, and (iii) an average structure representing the 50^{th} percentile of the overall dataset. Figure 4 (b) depicts the wall shape of these models. Table 3 shows a quantitative comparison of their performance. For a detailed understanding of the energy absorption mode related to the selected geometries, FEA and experiments are performed on them. Figure 4 (c-d) shows a comparison between the stress-strain response curves of the best-performing and worst-performing cell and the stress-strain curve of the benchmark model. The stresses are normalized to the absolute maximum value.

Comparing the numerical results with the experimental ones, their similarity first emerges, confirming the effectiveness of the approach used. On the other hand, analyzing the differences between the mechanical response of the individual structures, it can be seen that the honeycomb cell with the best performance is characterized by a low peak stress and a post-buckling deformation, which is almost perfectly plastic, ensuring energy absorption at a constant force. The worst honeycomb structure maximizes energy storage predominantly in the linear elastic regime and exhibits a noticeable drop after buckling. These results are in line with our expectation. In fact, to efficiently absorb a given amount of energy, the maximum force must be minimized, and the behavior of the honeycomb cell must be as close as possible to an elastic-perfectly plastic behavior[57]. The outcome of the proposed framework shows how this can be effectively achieved through the honeycomb cell wall shape tailoring.

Remarks. In this study, a data-driven biomimetic approach is proposed to customize the mechanical properties of architected materials by controlling buckling and post-critical behavior. Inspired by honeycomb-like structures found in diatom exoskeletons, which exhibit variable material distributions along the out-of-plane direction, we analyze the effect of their functional gradients on the energy absorption properties of millimeter-sized elastomeric structures that can be 3D printed. Despite the limited range of thickness distributions examined, by tailoring the shape of honeycomb cell walls, a performance increase of 250%, compared to the benchmark model with a constant wall thickness, is achieved. In contrast to most numerical data-driven approaches, which typically require significant computational power for both dataset creation and metamodeling training, this result is obtained using a standard implicit numerical solver and a commercial laptop. Therefore, the adopted framework shows great potential for the rapid and cost-effective design of innovative structures and materials for energy-absorbing applications such as helmets, sports impact protection, and packaging.

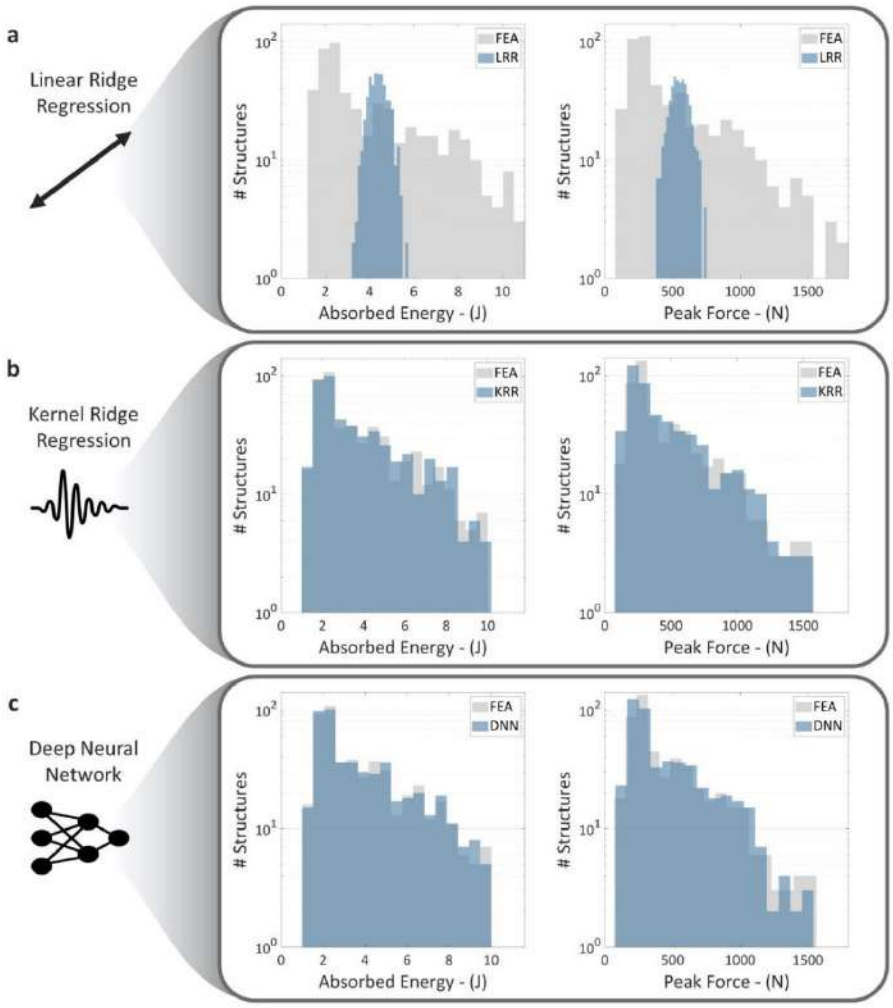

Figure 3. Absorbed energy and peak force distributions obtained from FEA analysis and predicted by three different machine learning algorithms on the test set. (a) Comparison between FEA and Linear Ridge Regression (LRR). (b) Comparison between FEA and Kernel Ridge Regression (KRR). (c) Comparison between FEA and Deep Neural Network (DNN).

Table 2. R^2 score of the Kernel Ridge Regression (KRR) and the Deep Neural Network (DNN). The table includes the overall R^2 calculated considering both the absorbed energy EA and the peak load F_{max}, the R^2 on the single metric on the 90th and 95th percentile to show the better tail reconstruction of the DNN in distribution tails.

ML algorithm	R^2 score				
	Overall	90th percentile		95th percentile	
		EA	F_{max}	EA	F_{max}
KRR	0.964	0.770	0.572	0.711	0.519
DNN	0.981	0.842	0.762	0.700	0.653

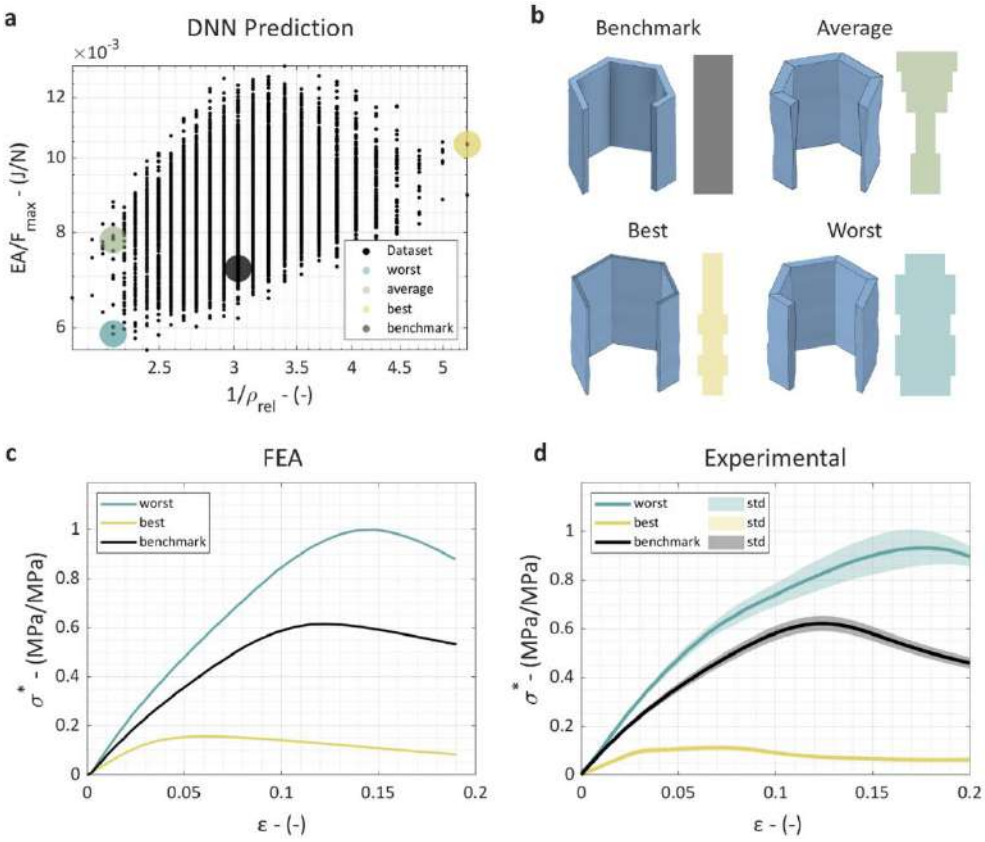

Figure 4. Predictions of the Deep Neural Network (DNN) and comparison with the benchmark solution. (a) Mechanical performance of bioinspired structures contained in the design space predicted by the DNN. Highlighted in the diagram: the benchmark model and three structures representative of the property variability induced by thickness gradients. (b) Representation of the geometry of the analyzed models with a focus on their cell wall thickness profiles. (c) Numerical and (d) experimental stress-strain curves of out-of-plane compression loading for the best, worst, and benchmark honeycomb cells.

Table 3. DNN prediction of absorbed energy, critical load, and performance parameter $EA/(\rho_{rel}F_{max})$ of the benchmark, best, average, and worst honeycomb cell; performance gain with respect to the benchmark structure.

Honeycomb	ρ_{rel} (-)	EA (J)	F_{max} (N)	$EA/(\rho_{rel}F_{max})$ (J/N)	Performance gain
Benchmark	0.33	7.88	1099.3	0.022	---
Best	0.19	1.56	149.5	0.055	254%
Average	0.29	2.37	303.4	0.027	122%
Worst	0.45	9.99	1697	0.013	60%

Although there is no doubt that geometric gradients in diatom exoskeletons are responsible for mechanical protection, this approach does not identify a match between the profile of the optimized cell and that of the algae. This mismatch can be mainly associated with the following reasons: (i) we focus only on the thickness gradient effect, neglecting other morphological aspects and using TPU as base material while diatom frustule is composed of amorphous biosilica; (ii) the frustule shapes are extremely complex and require a more sophisticated approach to be represented; (iii) the diatom exoskeleton is optimized to perform multiple functions at the same time and not only to absorb mechanical energy.

To generalize this study, the base material can be assumed as a design variable and tailored according to the specific application requirements (e.g., biocompatible metals for biomedicine, biodegradable polymers for sustainable design, nanocomposites for smart capabilities) or to further understand the biological role of the frustule (i.e., assuming silica-based ceramics). The interplay between different material failure modes and thickness gradients could provide additional insights to enhance honeycomb structural performance and broaden the range of functions they can fulfill. Also, alternative ways to describe the natural thickness gradients should be investigated. Since the problem of honeycomb out-of-plane elastic instability can be traced back to harmonic-type solutions[56,58], a promising idea is to assume

a space of parametric functions (*e.g.*, using Fourier series) to represent the functional gradients and build an AI model that can fit them to a set of diatom images to: (i) discover the most recurrent material distribution patterns, (ii) build a thickness profile generator that faithfully represents biological designs, and (iii) investigate the shape-property relationship in more detail. However, the success of such approach is highly dependent on the availability and quality of diatom data, which is very limited to date. A more versatile solution, on the other hand, is offered by language-based representations, as they apply to a variety of high-dimensional data and are independent of a priori knowledge of material design logic[36].

Nevertheless, we can still conclude that the thickness gradients featured in diatom cell walls allow one to improve the structural performance of the biological material. Indeed, one can notice the similarity of the natural cell shape with the shape of the average cell predicted by our framework, which already shows a 122% performance gain w.r.t. the benchmark honeycomb. It should also be noticed that periodic boundary conditions (PBCs) are not applied to the vertical edges of the honeycomb cells. Their absence does not allow us to recreate the mechanical behavior of the periodic material from a single cell analysis. Yet, it allows the study to be generalized in that: (i) by optimizing the performance of the single cell, a global improvement in the performance of the corresponding architected material can also be expected; (ii) the results obtained, besides being exploitable for the class of materials mentioned, can also be extended for modeling columns and rods designed against buckling.

There are several examples in the engineering field where a pointwise material design would improve dramatically the performance. A common example is given by prostheses, where a local material tuning is crucial to provide a more homogenous stress and strain distribution, reducing local concentrations. Another example is provided by sports protective equipment, such as helmets, pads, and other injury prevention devices (*e.g.*, body armor), where protection and lightness must coexist. These generally mutually exclusive characteristics can be combined by a targeted optimization of the structure, to have a mechanical response that at the same time limits the peak load and absorbs as much energy as possible to avoid severe injuries. Similar needs are encountered in the field of soft robotics. Especially when dealing with fragile objects it is fundamental that grippers do not exceed certain load limits. This can be achieved by implementing optimized architected materials that can significantly deform after reaching the critical load but, thanks to the use of elastomeric polymers, recover their shape when the load is removed.

To fully understand the shape-performance relationship in diatoms, a multidisciplinary approach is needed. As future developments we plan to expand the study by evaluating the multifunctionality of diatom-inspired architected materials, including fluid dynamical and optical performances in a multi-objective optimization framework.

EXPERIMENTAL SECTION

Biomimetic Design. We focus on the structural arrangement of the diatom exoskeleton frustule characteristic of the micrometer scale (Figure 1) and reminiscent of sandwich panels. To characterize the effect of shape heterogeneities occurring within the areolae on the out-of-plane compression loading scenario, different geometries of unit cells are studied: (i) a geometric benchmark model with constant-thickness walls and (ii) ~18000 models with varying wall thickness gradients. The former provides a benchmark with known mechanical behavior[58,59] for comparison with the geometrically tailored structures. The dimensions are defined on the millimeter scale, while maintaining the same proportions as the natural structure. Specifically, the edge length side of the mean perimeter defining the section of the hexagonal prismatic cell, the height of the latter, and the thickness of its walls are 14 mm, 28 mm, and 2 mm, respectively. This scale-up is necessary to cope with the limitations imposed by the AM technology used. From this model, we derive the other bioinspired structures through an algorithm that randomly defines the material distributions in the honeycomb walls, keeping the other geometric features unchanged (Figure 1 (d)). To limit the number of possible design solutions, we divide the benchmark unit cell into seven equal partitions along its height, then assign each one a thickness value belonging to the following vector t = [1.0 1.5 2.0 2.5 3.0] mm. This range of variation has been chosen so that the benchmark model represents an average configuration. We also impose a constraint on the gradient to avoid unphysical configuration. This is achieved by limiting to two steps the possible increments between two adjacent partitions. More details are available in the Supporting Information (SI) file.

Analytical Modeling. Honeycombs mechanical response under out-of-plane compression is characterized by three different stages (see Figure 1 (e)): (i) a first linear elastic regime; (ii) a region characterized by constant stresses known as the "plateau", triggered by buckling cell failure; and (iii) a densification phase in which the material becomes increasingly stiff due to the filling of voids contained within it associated with cell failure[58,59]. In the case of an elastomeric material, this mechanical behavior is also influenced by viscoelastic effects, thus on the loading rate. This study is limited to a quasi-static loading scenario. The honeycomb unit cell is assumed to have an elastic-perfectly plastic behavior; thus, it is described by the elastic modulus and the maximum force F_{max} estimated from the linearized buckling theory[58,59]. The honeycomb out-of-plane elastic properties are functions of its relative density ρ_{rel}[58,59]:

$$\rho_{rel}=\frac{A_{honey}}{A_{app}}\cong\frac{2}{\sqrt{3}}\frac{T}{L}=\frac{E_{honey}}{E_{bulk}} \quad (1)$$

where T and L represent the values of the wall thickness and the edge length, respectively, E_{honey} and E_{bulk} are the Young's moduli of the unit cell and of the bulk material, A_{honey} and A_{app} are the effective and the apparent cross-sectional area of the honeycomb cell. F_{max} can be calculated as:

$$F_{max}=3K\frac{E_{bulk}}{(1-\nu_{bulk}^2)}\frac{T^2}{L} \quad (2)$$

where K is a constraint factor dependent on the boundary conditions applied to the plates constituting the honeycomb cell walls[56] and ν_{bulk} is the Poisson's coefficient of the parent material. The value of the maximum stress is derived from F_{max} using the A_{app} section.

Finite Element Analysis (FEA). All the modeled cells have the same average surface area. To minimize the computational effort, this area is discretized through four-node shell elements with an average size of 0.5 mm, then the thickness associated with each element is locally adapted through a custom macro. The Blatz-Ko[60] hyperelastic material model, calibrated on the outcome of uniaxial tensile and compressive tests performed on 3D-printed samples, is adopted to describe the behavior of the TPU. The calibration phase is carried out using the commercial software PolymerFEM. Simulations are performed using an implicit approach, based on the Newton-Raphson method for calculating the nonlinear solution. The bottom and top bases of each cell are placed in contact with two rigid surfaces (representing the compression plates of the testing machine). The top surface is moved axially at a slow speed to induce quasi-static compression, while the bottom surface is kept fixed. Contact interactions are modeled using a pair-based definition using target segment and line-to-surface elements in ANSYS. A friction coefficient of 1.2 is used to simulate sliding between the rigid surfaces and the FE mesh. For each cell, a single load step is applied, and the vertical displacement of the upper base is calculated at each substep, obtaining the force-displacement curve for large displacements. From the latter, the stress-strain relationship is derived, and the energy absorption properties are calculated. The number of substeps is adjusted by the program according to the solution gradient.

Supervised Learning. The numerical dataset used for the ML algorithm tuning is divided into three parts: (i) training set (1000 data), (ii) validation set (500 data), and (iii) test set (500 data). The training set is used to make the ML algorithms learn the parameters that define the regression models (*i.e.*, the link between the input thickness distribution, x_i, and the output mechanical properties, y_i). The validation and the test set are used to tune their hyperparameters and evaluate their goodness of approximation, respectively. The optimal metamodel is defined and then used to calculate the mechanical properties of the non-simulated geometric models (about 16000). Figure 5 depicts the adopted workflow. To enhance the performance of ML algorithms, both the labels and features are normalized and centered. These transformations ensure that all data points have a mean value of zero and are normalized to one. Also, the 2000 structures are selected randomly to avoid any bias. Three different supervised learning approaches are used and compared:

- *Linear Ridge Regression (LRR).* Thanks to its simplicity and computational efficiency, a linear regression is adopted as initial approximation tool. For its implementation, we use the related Scikit-learn package choosing a regularization parameter α=0.1 to prevent underfitting.
- *Kernel Ridge Regression (KRR).* Nonlinear kernel algorithms allow capturing complex input-output relationships while maintaining high computational efficiency. Here we define a kernel regression model based on radial basis functions by exploiting Scikit-learn. In this case, the regularization-related hyperparameter is optimized by cross-validation, varying it on a logarithmic scale in the interval $[10^{-6}, 10^{1}]$ and choosing the optimal one (Figure S3).
- *Deep Neural Network (DNN).* DNNs have no limits in terms of capability to approximate functions[61], however, compared to previous approaches they require significantly more computational effort for training and hyperparameters selection, due to the large number of parameters and hyperparameters to be tuned. We create our own DNN using Keras, a user-friendly front-end API for TensorFlow. About fifty different DNN architectures are analyzed, with different combinations of hyperparameters (*i.e.*, number of hidden layers, number of neurons in each hidden layer, dropout fraction for each layer) to maximize the fitting. Detailed information is reported in the SI file. The selected DNN architecture consists of an input layer with seven neurons (one for each thickness partition), an output layer with two neurons (one for each label: EA and F_{max}), and five fully connected hidden layers. The first and last hidden layers have 32 and 128 neurons, respectively, while the three central layers have 256 neurons. We use the ReLU activation function for all the layers except for the output one, where we implement the 'linear' activation function commonly employed for regression tasks. Finally, to minimize the loss function, we utilize the Adam optimization algorithm. Training the DNN and its parameters involves running a total of 50 epochs with a batch size of 200.

For all three ML models, we evaluate the goodness of the fit using the R^2 score, which represents the fraction of information reconstructed by the model. The algorithms are run using Google Colab.

3D Printing and Testing. The Fused Filament Fabrication (FFF) technology 3D printer Original Prusa i3 MK2s is used to manufacture both the specimens needed for TPU mechanical characterization and the honeycomb cell samples with geometric and non-geometric tailoring. A minimum number of three samples per test and geometry is considered, to ensure repeatability of results. The process parameters are provided in SI. For all the samples, the commercial filament FILOALFA® ALFA TPU hard is used. To calibrate the hyperelastic model of TPU, both tensile and compression tests are carried out, according to ASTM D412 and ASTM D575 standards[62,63], respectively. To experimentally assess the behavior of honeycomb cells, we carry out quasi-static compression tests in displacement control (with a crosshead speed v=2mm/min), using a ZwickRoell ProLine universal testing machine endowed with a 10 kN load cell.

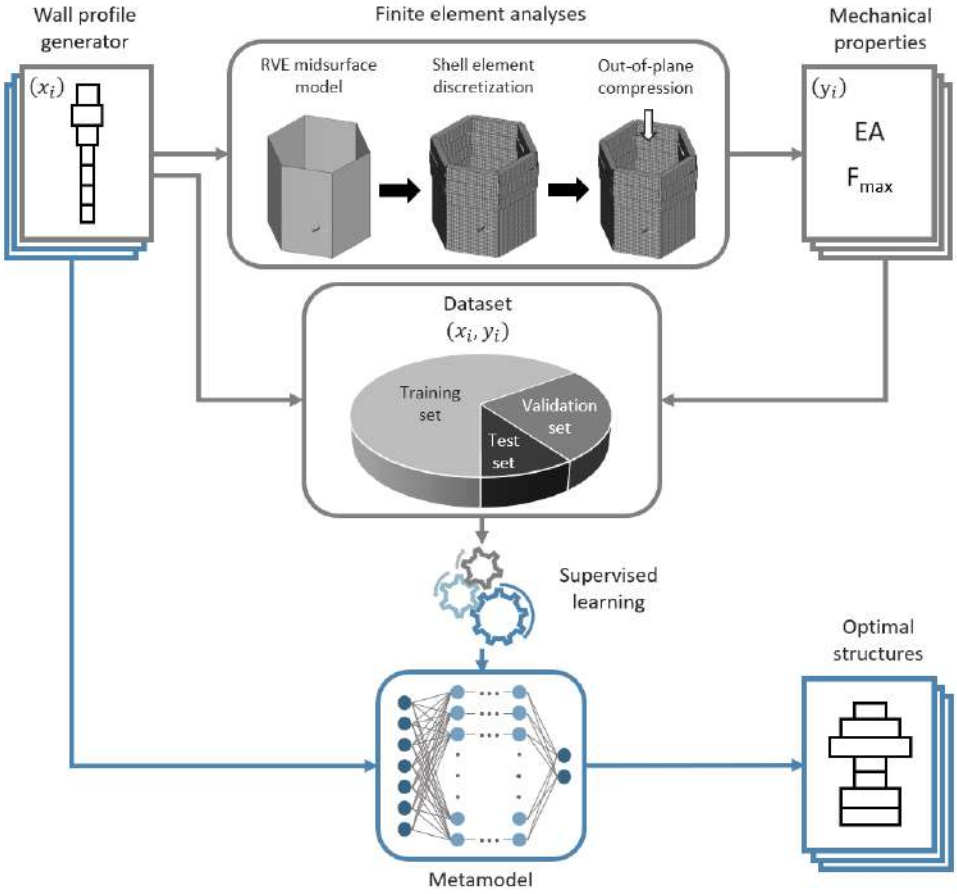

Figure 5. Schematic of the workflow used to build the numerical dataset, train the machine learning algorithms, and predict the behavior of geometrically tailored honeycomb cells. The design space, consisting of approximately eighteen thousand different structures, is defined by creating seven-component vectors, x_i, describing the wall thickness distribution. Two thousand structures are randomly selected and analyzed by FEA to obtain the 2D vector, y_i, characterizing the energy absorption capacity of the structure: energy absorbed (EA) and peak load (F_{max}). The metamodel built by supervised learning algorithms is trained, tuned, and tested on the dataset. The mechanical properties of the geometric models, not included in the dataset, are predicted, and those with the optimal performance identified.

ASSOCIATED CONTENT

Supporting Information

The Supporting Information (SI) file contains geometric details of the bioinspired model used as a benchmark for numerical model validation; 3D printing process parameters; additional information on machine learning algorithms. This material is available free of charge via the Internet at http://pubs.acs.org

AUTHOR INFORMATION

Corresponding Author

*Flavia Libonati - University of Genoa, Polytechnic School, Department of Mechanical, Energy, Management and Transportation Engineering, Via all'Opera Pia 15/A, 16145, Genova, Italy; orcid.org/0000-0001-6490-1922; Email: flavia.libonati@unige.it

ACKNOWLEDGMENTS

The authors acknowledge support from the University of Genoa, under the Curiosity Driven Starting Grant initiative.

ABBREVIATIONS

AM, Additive Manufacturing; ML, Machine Learning; FEA, Finite Element Analysis; TPU, thermoplastic polyurethane; LRR, Linear Ridge Regression; KRR, Kernel Ridge Regression; DNN, Deep Neural Network; PBCs, Periodic Boundary Conditions.

REFERENCES

(1) Benedetti, M.; du Plessis, A.; Ritchie, R. O.; Dallago, M.; Razavi, S. M. J.; Berto, F. Architected Cellular Materials: A Review on Their Mechanical Properties towards Fatigue-Tolerant Design and Fabrication. *Mater. Sci. Eng. R Reports* **2021**, *144*, 100606. https://doi.org/10.1016/j.mser.2021.100606.

(2) Schaedler, T. A.; Carter, W. B. Architected Cellular

Materials. *Annu. Rev. Mater. Res.* **2016**, *46*, 187–210. https://doi.org/10.1146/annurev-matsci-070115-031624.
(3) Kladovasilakis, N.; Tsongas, K.; Karalekas, D.; Tzetzis, D. Architected Materials for Additive Manufacturing: A Comprehensive Review. *Materials (Basel).* **2022**, *15*, 1–18. https://doi.org/10.3390/ma15175919.
(4) Osanov, M.; Guest, J. K. Topology Optimization for Architected Materials Design. *Annu. Rev. Mater. Res.* **2016**, *46*, 211–233. https://doi.org/10.1146/annurev-matsci-070115-031826.
(5) Musenich, L.; Libonati, F. Damage and Failure Mechanisms of Biological Materials. In *Reference Module in Materials Science and Materials Engineering*; Elsevier, 2022; pp 2–40. https://doi.org/10.1016/b978-0-12-822944-6.00015-3.
(6) Vincent, J. F. V. Biomimetics - A Review. *Proc. Inst. Mech. Eng. Part H J. Eng. Med.* **2009**, *223*, 919–939. https://doi.org/10.1243/09544119JEIM561.
(7) Fratzl, P. Biomimetic Materials Research: What Can We Really Learn from Nature's Structural Materials? *J. R. Soc. Interface* **2007**, *4*, 637–642. https://doi.org/10.1098/rsif.2007.0218.
(8) Libonati, F.; Buehler, M. J. Advanced Structural Materials by Bioinspiration. *Advanced Engineering Materials*. 2017. https://doi.org/10.1002/adem.201600787.
(9) Mead, T.; Jeanrenaud, S. The Elephant in the Room: Biomimetics and Sustainability? *Bioinspired, Biomim. Nanobiomaterials* **2016**, *6*, 113–121. https://doi.org/10.1680/jbibn.16.00012.
(10) Barthelat, F. Architectured Materials in Engineering and Biology: Fabrication, Structure, Mechanics and Performance. *Int. Mater. Rev.* **2015**, *60*, 413–430. https://doi.org/10.1179/1743280415Y.0000000008.
(11) Ritchie, R. O. The Conflicts between Strength and Toughness. *Nat. Mater.* **2011**, *10*, 817–822. https://doi.org/10.1038/nmat3115.
(12) Eder, M.; Amini, S.; Fratzl, P. *Biological Composites—Complex Structures for Functional Diversity*; 2018; Vol. 362. https://doi.org/10.1126/science.aat8297.
(13) Marth, J. D. A Unified Vision of the Building Blocks of Life. *Nature Cell Biology*. 2008, p 1015. https://doi.org/10.1038/ncb0908-1015.
(14) Liu, Z.; Zhang, Z.; Ritchie, R. O. Structural Orientation and Anisotropy in Biological Materials: Functional Designs and Mechanics. *Adv. Funct. Mater.* **2020**, *30*, 1–17. https://doi.org/10.1002/adfm.201908121.
(15) Huang, W.; Restrepo, D.; Jung, J. Y.; Su, F. Y.; Liu, Z.; Ritchie, R. O.; McKittrick, J.; Zavattieri, P.; Kisailus, D. Multiscale Toughening Mechanisms in Biological Materials and Bioinspired Designs. *Adv. Mater.* **2019**, *31*, 1–37. https://doi.org/10.1002/adma.201901561.
(16) Liu, Z.; Meyers, M. A.; Zhang, Z.; Ritchie, R. O. Functional Gradients and Heterogeneities in Biological Materials: Design Principles, Functions, and Bioinspired Applications. *Prog. Mater. Sci.* **2017**, *88*, 467–498. https://doi.org/10.1016/j.pmatsci.2017.04.013.
(17) Naleway, S. E.; Porter, M. M.; McKittrick, J.; Meyers, M. A. Structural Design Elements in Biological Materials: Application to Bioinspiration. *Adv. Mater.* **2015**, *27*, 5455–5476. https://doi.org/10.1002/adma.201502403.
(18) Dunlop, J. W. C.; Weinkamer, R.; Fratzl, P. Artful Interfaces within Biological Materials. *Mater. Today* **2011**, *14*, 70–78. https://doi.org/10.1016/S1369-7021(11)70056-6.
(19) Ren, J.; Wang, Y.; Yao, Y.; Wang, Y.; Fei, X.; Qi, P.; Lin, S.; Kaplan, D. L.; Buehler, M. J.; Ling, S. Biological Material Interfaces as Inspiration for Mechanical and Optical Material Designs. **2019**. https://doi.org/10.1021/acs.chemrev.9b00416.
(20) Jia, Z.; Deng, Z.; Li, L. Biomineralized Materials as Model Systems for Structural Composites: 3D Architecture. *Adv. Mater.* **2022**, *34*. https://doi.org/10.1002/adma.202106259.
(21) Ackbarow, T.; Buehler, M. J. Hierarchical Coexistence of Universality and Diversity Controls Robustness and Multi-Functionality in Protein Materials. *J. Comput. Theor. Nanosci.* **2008**, *5*, 1193–1204. https://doi.org/10.1166/jctn.2008.2554.
(22) Harris, J.; Böhm, C. F.; Wolf, S. E. Universal Structure Motifs in Biominerals: A Lesson from Nature for the Efficient Design of Bioinspired Functional Materials. *Interface Focus* **2017**, *7*. https://doi.org/10.1098/rsfs.2016.0120.
(23) Cranford, S. W.; Buehler, M. J. *Biomateriomics*; Springer Dordrecht, 2012. https://doi.org/10.1007/978-94-007-1611-7.
(24) Libonati, F.; Gu, G. X.; Qin, Z.; Vergani, L.; Buehler, M. J. Bone-Inspired Materials by Design: Toughness Amplification Observed Using 3D Printing and Testing. *Adv. Eng. Mater.* **2016**, *18*, 1354–1363. https://doi.org/10.1002/adem.201600143.
(25) Wegst, U. G. K.; Bai, H.; Saiz, E.; Tomsia, A. P.; Ritchie, R. O. Bioinspired Structural Materials. *Nat. Mater.* **2015**, *14*, 23–36. https://doi.org/10.1038/nmat4089.
(26) Sanders, E. D.; Pereira, A.; Paulino, G. H. Optimal and Continuous Multilattice Embedding. *Sci. Adv.* **2021**, *7*, 1–14. https://doi.org/10.1126/sciadv.abf4838.
(27) Meza, L. R.; Zelhofer, A. J.; Clarke, N.; Mateos, A. J.; Kochmann, D. M.; Greer, J. R. Resilient 3D Hierarchical Architected Metamaterials. *Proc. Natl. Acad. Sci. U. S. A.* **2015**, *112*, 11502–11507. https://doi.org/10.1073/pnas.1509120112.
(28) Olson, G. B. Computational Design of Hierarchically Structured Materials. *Science (80-.).* **1997**, *277*, 1237–1242. https://doi.org/10.1126/science.277.5330.1237.
(29) Morgan, D.; Jacobs, R. Opportunities and Challenges for Machine Learning in Materials Science. *Annu. Rev. Mater. Res.* **2020**, *50*, 71–103. https://doi.org/10.1146/annurev-matsci-070218-010015.
(30) Himanen, L.; Geurts, A.; Foster, A. S.; Rinke, P. Data-Driven Materials Science: Status, Challenges, and Perspectives. *Adv. Sci.* **2019**, *6*. https://doi.org/10.1002/advs.201900808.
(31) Guo, K.; Yang, Z.; Yu, C. H.; Buehler, M. J. Artificial Intelligence and Machine Learning in Design of Mechanical Materials. *Mater. Horizons* **2021**, *8*, 1153–1172. https://doi.org/10.1039/d0mh01451f.
(32) Bock, F. E.; Aydin, R. C.; Cyron, C. J.; Huber, N.; Kalidindi, S. R.; Klusemann, B. A Review of the Application of Machine Learning and Data Mining Approaches in Continuum Materials Mechanics. *Front. Mater.* **2019**, *6*.

https://doi.org/10.3389/fmats.2019.00110.
(33) Chen, C. T.; Gu, G. X. Machine Learning for Composite Materials. *MRS Commun.* **2019**, *9*, 556–566. https://doi.org/10.1557/mrc.2019.32.
(34) Agrawal, A.; Choudhary, A. Deep Materials Informatics: Applications of Deep Learning in Materials Science. *MRS Commun.* **2019**, *9*, 779–792. https://doi.org/10.1557/mrc.2019.73.
(35) Lew, A. J.; Buehler, M. J. Single-Shot Forward and Inverse Hierarchical Architected Materials Design for Nonlinear Mechanical Properties Using an Attention-Diffusion Model. *Mater. Today* **2023**, *64*, 10–20. https://doi.org/10.1016/j.mattod.2023.03.007.
(36) Buehler, M. J. MeLM, a Generative Pretrained Language Modeling Framework That Solves Forward and Inverse Mechanics Problems. *J. Mech. Phys. Solids* **2023**, *181*, 105454. https://doi.org/10.1016/j.jmps.2023.105454.
(37) Luu, R. K.; Buehler, M. J. Materials Informatics Tools in the Context of Bio-Inspired Material Mechanics. *J. Appl. Mech.* **2023**, *90*. https://doi.org/10.1115/1.4062310.
(38) Darouich, O.; Baaziz, W.; Ihiawakrim, D.; Hirlimann, C.; Spehner, D.; Schultz, P.; Poncet, H.; Rouchon, V.; Labidi, S.; Petit, C.; Levitz, P.; Ersen, O. 3D Multiscale Analysis of the Hierarchical Porosity in Coscinodiscus Sp. Diatoms Using a Combination of Tomographic Techniques†. *Nanoscale Adv.* **2022**, *4*, 1587–1598. https://doi.org/10.1039/d1na00691f.
(39) Zgłobicka, I.; Gluch, J.; Liao, Z.; Werner, S.; Guttmann, P.; Li, Q.; Bazarnik, P.; Plocinski, T.; Witkowski, A.; Kurzydlowski, K. J. Insight into Diatom Frustule Structures Using Various Imaging Techniques. *Sci. Rep.* **2021**, *11*, 1–10. https://doi.org/10.1038/s41598-021-94069-9.
(40) Xing, Y.; Yu, L.; Wang, X.; Jia, J.; Liu, Y.; He, J.; Jia, Z. Characterization and Analysis of Coscinodiscus Genus Frustule Based on FIB-SEM. *Prog. Nat. Sci. Mater. Int.* **2017**, *27*, 391–395. https://doi.org/10.1016/j.pnsc.2017.04.019.
(41) Aitken, Z. H.; Luo, S.; Reynolds, S. N.; Thaulow, C.; Greer, J. R. Microstructure Provides Insights into Evolutionary Design and Resilience of Coscinodiscus Sp. Frustule. *Proc. Natl. Acad. Sci. U. S. A.* **2016**, *113*, 2017–2022. https://doi.org/10.1073/pnas.1519790113.
(42) Schmid, A. M.; Volcani, B. E. Wall Morphogenesis in Coscinodiscus Wailesii Gran and Angst. I. Valve Morphology and Development of Its Architecture. *Journal of Phycology*. 1983, pp 387–402. https://doi.org/10.1111/j.0022-3646.1983.00387.x.
(43) Naleway, S. E.; Taylor, J. R. A.; Porter, M. M.; Meyers, M. A.; McKittrick, J. Structure and Mechanical Properties of Selected Protective Systems in Marine Organisms. *Mater. Sci. Eng. C* **2016**, *59*, 1143–1167. https://doi.org/10.1016/j.msec.2015.10.033.
(44) Hamm, C. E.; Merkel, R.; Springer, O.; Jurkojc, P.; Maiert, C.; Prechtelt, K.; Smetacek, V. Architecture and Material Properties of Diatom Shells Provide Effective Mechanical Protection. *Nature* **2003**, *421*, 841–843. https://doi.org/10.1038/nature01416.
(45) Gutiérrez, A.; Gordon, R.; Dávila, L. P. Deformation Modes and Structural Response of Diatom Frustules. *J. Mater. Sci. Eng. with Adv. Technol.* **2017**, *15*, 105–134. https://doi.org/10.18642/jmseat_7100121810.
(46) Gutiérrez, A.; Guney, M. G.; Fedder, G. K.; Dávila, L. P. The Role of Hierarchical Design and Morphology in the Mechanical Response of Diatom-Inspired Structures: Via Simulation. *Biomater. Sci.* **2018**, *6*, 146–153. https://doi.org/10.1039/c7bm00649g.
(47) Moreno, M. D.; Ma, K.; Schoenung, J.; Dávila, L. P. An Integrated Approach for Probing the Structure and Mechanical Properties of Diatoms: Toward Engineered Nanotemplates. *Acta Biomater.* **2015**, *25*, 313–324. https://doi.org/10.1016/j.actbio.2015.07.028.
(48) Pančić, M.; Torres, R. R.; Almeda, R.; Kiørboe, T. Silicified Cell Walls as a Defensive Trait in Diatoms. *Proc. R. Soc. B Biol. Sci.* **2019**, *286*. https://doi.org/10.1098/rspb.2019.0184.
(49) Michels, J.; Vogt, J.; Gorb, S. N. Tools for Crushing Diatoms - Opal Teeth in Copepods Feature a Rubber-like Bearing Composed of Resilin. *Sci. Rep.* **2012**, *2*, 1–6. https://doi.org/10.1038/srep00465.
(50) Buehler, M. J. Diatom-Inspired Architected Materials Using Language-Based Deep Learning: Perception, Transformation and Manufacturing. **2023**, 1–9. https://doi.org/https://doi.org/10.48550/arXiv.2301.05875.
(51) Noren, A. K. Characterization of Structure and Optical Properties of Diatoms for Improved Solar Cell Efficiency, 2011. http://hdl.handle.net/11250/248947.
(52) Li, K.; Li, Y.; Wang, X.; Cui, M.; An, B.; Pu, J.; Liu, J.; Zhang, B.; Ma, G.; Zhong, C. Diatom-Inspired Multiscale Mineralization of Patterned Protein-Polysaccharide Complex Structures. *Natl. Sci. Rev.* **2021**, *8*, 1–12. https://doi.org/10.1093/nsr/nwaa191.
(53) Kumar, S.; Ubaid, J.; Abishera, R.; Schiffer, A.; Deshpande, V. S. Tunable Energy Absorption Characteristics of Architected Honeycombs Enabled via Additive Manufacturing. *ACS Appl. Mater. Interfaces* **2019**, *11*, 42549–42560. https://doi.org/10.1021/acsami.9b12880.
(54) Andrew, J. J.; Ubaid, J.; Hafeez, F.; Schiffer, A.; Kumar, S. Impact Performance Enhancement of Honeycombs through Additive Manufacturing-Enabled Geometrical Tailoring. *Int. J. Impact Eng.* **2019**, *134*, 103360. https://doi.org/10.1016/j.ijimpeng.2019.103360.
(55) Clough, E. C.; Plaisted, T. A.; Eckel, Z. C.; Cante, K.; Hundley, J. M.; Schaedler, T. A. Elastomeric Microlattice Impact Attenuators. *Matter* **2019**, *1*, 1519–1531. https://doi.org/10.1016/j.matt.2019.10.004.
(56) Timoshenko, S. P.; Gere, J. M. *Theroy of Elastic Stability*; 1963.
(57) Avalle, M.; Belingardi, G.; Montanini, R. Characterization of Polymeric Structural Foams under Compressive Impact Loading by Means of Energy-Absorption Diagram. *Int. J. Impact Eng.* **2001**, *25*, 455–472. https://doi.org/10.1016/S0734-743X(00)00060-9.
(58) Zhang, J.; Ashby, M. F. The Out-of-Plane Properties of Honeycombs. *Int. J. Mech. Sci.* **1992**, *34*, 475–489. https://doi.org/10.1016/0020-7403(92)90013-7.
(59) Gibson, L. J.; Ashby, M. F. *Cellular Solids: Structure and Properties, Second Edition*; Cambridge University Press, 2014. https://doi.org/10.1017/CBO9781139878326.

(60) Blatz, P. J.; Ko, W. L. Application of Finite Elastic Theory to the Deformation of Rubbery Materials. *Trans. Soc. Rheol.* **1962**, *6*, 223–252. https://doi.org/10.1122/1.548937.
(61) Hornik, K.; Stinchcombe, M.; White, H. Multilayer Feedforward Networks Are Universal Approximators. *Neural Networks* **1989**, *2*, 359–366. https://doi.org/10.1016/0893-6080(89)90020-8.
(62) Gooch, J. W. ASTM D412-15 Standard Test Methods for Vulcanized Rubber and Thermoplastic Elastomers. *Annual Book of ASTM Standards*, 2011, 1–14. https://doi.org/10.1520/D0412-98AR02E01.
(63) ASTM. *ASTM D575 – 91 (Reapproved 2012) Standard Test Methods for Rubber Properties in Compression or Shear*; 2012; Vol. XIII. https://doi.org/10.1520/D0575-91R12.

Supporting Information

Tunable energy absorption in 3D-printed data-driven diatom-inspired architected materials

Ludovico Musenich, Alessandro Stagni, Lucio Derin, Flavia Libonati*
University of Genoa
Department of Mechanical, Energy, Management and Transportation Engineering,
Via all'Opera Pia 15/A, 16145, Genova, Italy

*Corresponding author: flavia.libonati@unige.it

1 Geometric details of the bioinspired model used as a benchmark for numerical model validation

Figure S1 shows the geometry of the benchmark unit cell. The honeycomb dimensions - shown in **Table S1** - are chosen (i) by respecting the proportions of the natural frustule structure of *Coscinodiscus sp.* diatoms, obtained by averaging the data available in the literature [1]–[5]; (ii) to ensure the fabrication of samples for additive manufacturing and perform experimental compression tests.

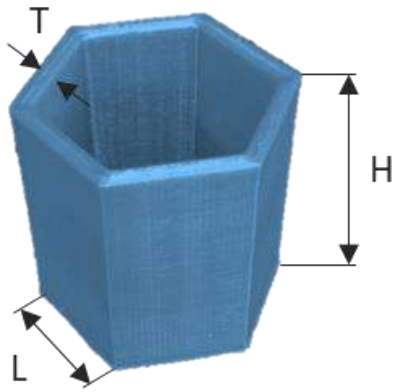

Figure S1 – Benchmark honeycomb cell used for the validation of FE model.

Table S1 - Dimensions of the benchmark honeycomb model.

Unit cell geometric parameter	Symbol	Value (mm)
Height	H	28
Edge length	L	14
Walls thickness	T	2

2 Algorithms for the calculation of the possible geometries

The pseudo-code of the structure generator algorithm is the following:

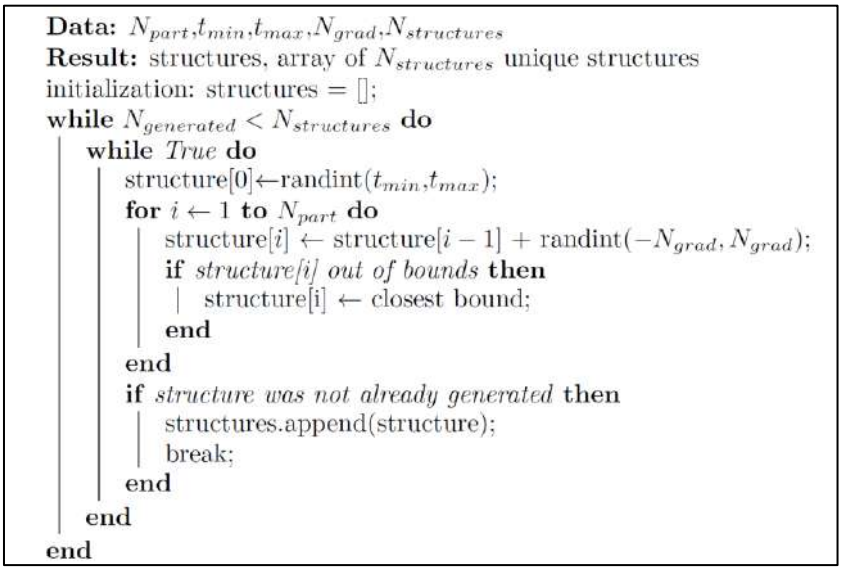

Figure S2 – Structure generator algorithm pseudo-code. N_{part} is the number of vertical partitions of the wall; t_{min}, t_{max} are the minimum and maximum thickness value per partition (the step is supposed to be 1); N_{grad} is the maximum number of steps between one partition and its neighbors (maximum gradient of the wall profile); $N_{structures}$ is the number of structures to be generated; randint(i,j) are functions that uniformly extracts an integer between i and j included.

3 3D Printing

Table S2 - 3D printing process parameters used for TPU specimens.

Process parameter	Unit	Value
Extruder temperature	°C	230
Max printing speed	mm/s	40
Printer bed temperature	°C	50
Drying temperature	°C	70
Drying time	hours	5
Infill percentage	%	100
Other parameters	-	Prusa slicer default values

4 Machine Learning Algorithms

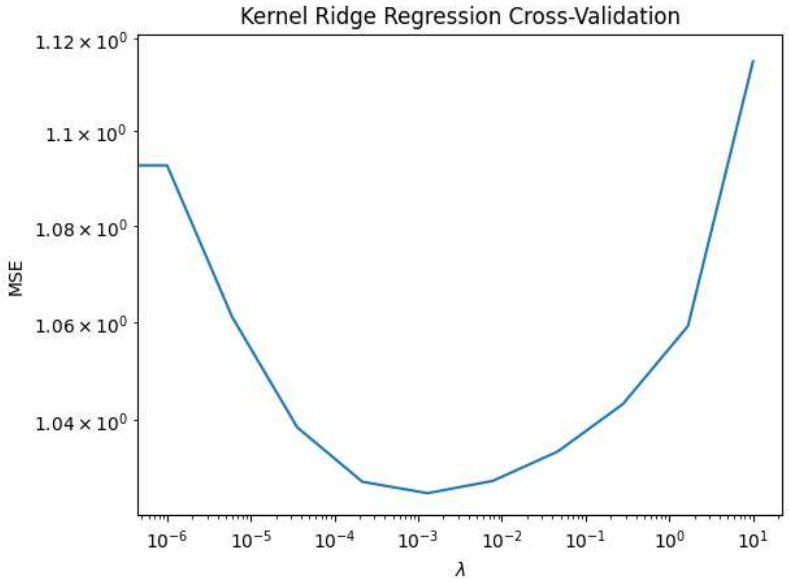

Figure S3 – Kernel Ridge Regression cross-validation. As we can observe from the graph reporting the Mean Square Error (MSE) on the validation set versus the regularization parameter (λ), the model exhibits the classical bias-variance behavior of the validation error, allowing for the best value of the hyperparameter λ, defined as the global minimum of the validation error itself. The best value guarantees a good trade-off between the bias (underfitting) and variance (overfitting) components of the validation error, making the model as descriptive and simultaneously as robust as possible.

Table S3 – DNN hyperparameters analyzed with the relative values.

DNN Hyperparameter	Analyzed values
Number of hidden layers	4, 8, 16, 32
Number of neurons per hidden layer	32, 64, 128, 256
Dropout function	0.1, 0.01, 0
Total DNN model analyzed	48

Despite good stability of the overall performances of the DNNs, with the worst model R2 score being only 4% less than the optimal one, the fitting of the metamodels on the distribution tails is highly sensible to the hyperparameters choice. Analyzing the R^2 score on the 90^{th} percentile there is a difference of about 60% between the best and the worst-performing DNN.

Table S4 - Performance comparison between the finite element end machine learning algorithms.

Model	Analysis description	Structure analyzed	CPU time*		"Accuracy"
FEM	FE non-linear analysis	2000	6	h	Deterministic
LRR	Validation set	1000	N/A		R^2= 0.567
	Test set prediction	500	N/A		N/A**
KRR	Validation set	1000	0.3	s	R^2=0.975
	Test set prediction	500	0.1	s	R^2=0.964
DNN	Validation set	1000	75	s	R^2=0.984
	Test set prediction	500	0.1	s	R^2=0.981
	Prediction	16000	0.1	s	N/A

**ML algorithms are run on Google Colab without GPU acceleration. CPU time are comparable with workstation.*

***Not Available due to the poor fitting on the validation set*

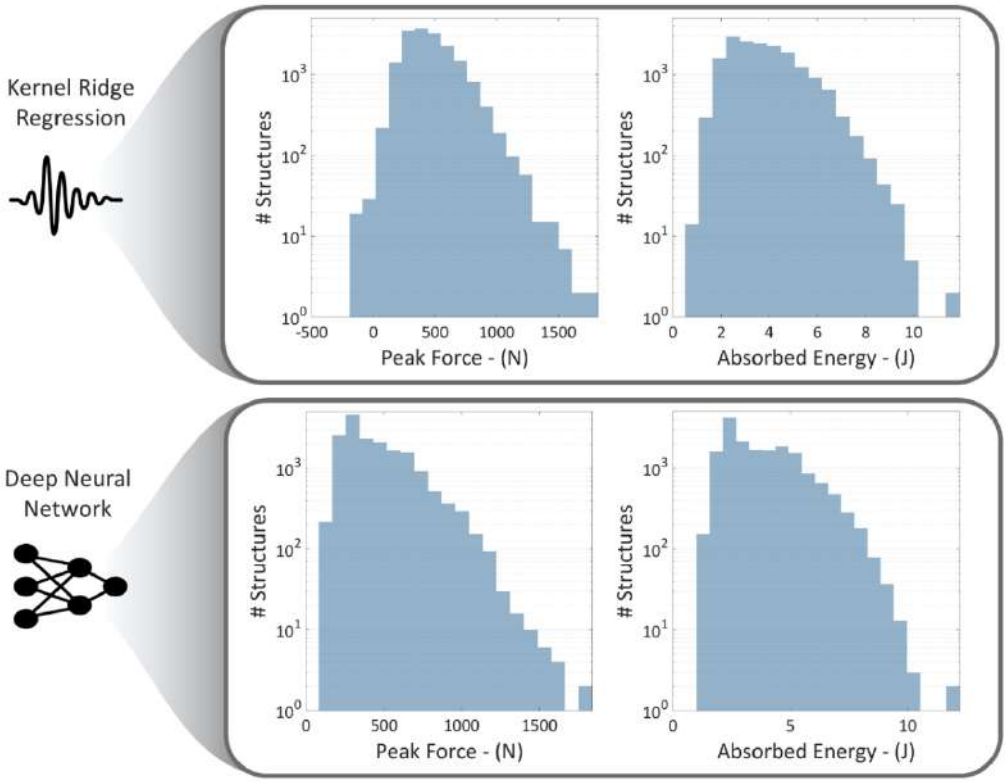

Figure S4 - Prediction results of the KRR and DNN algorithms on the entire dataset.

References

[1] O. Darouich *et al.*, “3D multiscale analysis of the hierarchical porosity in Coscinodiscus sp. diatoms using a combination of tomographic techniques†,” *Nanoscale Adv.*, vol. 4, no. 6, pp. 1587–1598, 2022, doi: 10.1039/d1na00691f.

[2] Y. Xing *et al.*, “Characterization and analysis of Coscinodiscus genus frustule based on FIB-SEM,” *Prog. Nat. Sci. Mater. Int.*, vol. 27, no. 3, pp. 391–395, 2017, doi: 10.1016/j.pnsc.2017.04.019.

[3] Z. H. Aitken, S. Luo, S. N. Reynolds, C. Thaulow, and J. R. Greer, “Microstructure provides insights into evolutionary design and resilience of Coscinodiscus sp. frustule,” *Proc. Natl. Acad. Sci. U. S. A.*, vol. 113, no. 8, pp. 2017–2022, 2016, doi: 10.1073/pnas.1519790113.

[4] D. Losic, G. Rosengarten, J. G. Mitchell, and N. H. Voelcker, “Pore architecture of diatom frustules: Potential nanostructured membranes for molecular and particle separations,” *J. Nanosci. Nanotechnol.*, vol. 6, no. 4, pp. 982–989, 2006, doi: 10.1166/jnn.2006.174.

[5] A. Gibaud *et al.*, “Analysis of diatoms by holotomography,” *Surfaces and Interfaces*, vol. 17, no. July, p. 100358, 2019, doi: 10.1016/j.surfin.2019.100358.

[6] M. F. Gibson, Lorna J., Ashby, *Cellular Solids: Structure and Propertes.* Cambridge University Press, 1988.

[7] J. Zhang and M. F. Ashby, “The out-of-plane properties of honeycombs,” *Int. J. Mech. Sci.*, vol. 34, no. 6, pp. 475–489, 1992, doi: 10.1016/0020-7403(92)90013-7.